

Opposite amplitude–phase entropy responses at a non-Hermitian avoided crossing

Kyu-Won Park,^{1,*} Soojoon Lee,^{1,2,†} and Kabgyun Jeong^{3,2,‡}

¹*Department of Mathematics and Research Institute for Basic Sciences, Kyung Hee University, Seoul, 02447, Korea*

²*School of Computational Sciences, Korea Institute for Advanced Study, Seoul 02455, Korea*

³*Research Institute of Mathematics, Seoul National University, Seoul 08826, Korea*

(Dated: February 4, 2026)

Avoided crossings (A.C.) in open resonators arise from non-Hermitian mode interaction, where leakage produces complex spectra and biorthogonal eigenmodes. Intensity-based entropies are robust markers of mode mixing but discard the phase structure of the complex field. Here we introduce a field-level information-theoretic analysis based on the joint statistics of local amplitude and phase under Born-weighted sampling on the cavity grid. For an open elliptical microcavity in the strong-interaction A.C. regime, we find a distinctive sector-resolved response: amplitude statistics tighten while phase statistics broaden maximally at the mixing point, and conditioning reveals strong amplitude–phase dependence. By introducing a coarse position label and the associated co-information, we further show that the enhancement of global amplitude–phase coupling is strongly shaped by spatial heterogeneity across the cavity.

PACS numbers:

INTRODUCTION

Open resonators and wave systems are intrinsically non-Hermitian: coupling to an external environment produces irreversible leakage, complex resonance spectra, and biorthogonal eigenmodes [1–3]. Such effective non-Hermitian descriptions can be derived by eliminating environmental degrees of freedom using projection-operator approaches [4]. In this setting, near-degeneracies are not only spectral features but also involve qualitative changes in eigenmode structure, especially near exceptional points (EPs) where eigenvalues and eigenmodes coalesce [5–7]. Recent progress has further clarified how non-Hermiticity reshapes spectral geometry and topology across platforms [8–10].

Open dielectric microcavities offer a clean photonic platform for exploring such effects because radiative loss is intrinsic and can be tuned continuously by shape deformation [11–13]. In parallel, non-Hermitian photonics has rapidly expanded to include topological and device-level directions, supported by recent reviews and tutorials [14–16]. Landmark experiments have demonstrated exceptional rings, dynamical encircling, and microcavity sensing at EPs [17–19]. Current trends emphasize practical constraints and noise-aware interpretations of EP-based sensing and functionality [20–22].

A widely used way to characterize mode interaction is through the intensity distribution and its real-space delocalization. Across an avoided crossing (A.C.), intensity patterns typically hybridize and exchange modal character, and intensity-based entropies provide robust signatures of this redistribution [23–25]. However, intensity is a gauge-invariant observable that discards the phase structure of the complex eigenfield and is therefore insensitive to non-Hermitian features that reside in the phase and in eigenmode non-orthogonality. This moti-

vates a complementary, field-level diagnostic that keeps the full complex eigenmode.

In this work we develop an information-theoretic framework that treats the local amplitude and phase of the complex field as statistical variables induced by intensity-weighted sampling on the cavity grid. This construction allows us to track how amplitude and phase statistics reshape across the A.C. and to quantify their dependence through marginal and conditional measures, using standard information-theoretic tools and estimators [25–27]. Applying the framework to an open elliptical microcavity, we identify a distinctive signature of the A.C. that cannot be inferred from intensity alone: the amplitude statistics tighten at the mixing point, while the phase statistics broaden maximally, and conditioning shows that amplitude and phase remain strongly coupled in the interaction window. The resonant fields used for our analysis are computed for open dielectric cavities using boundary-integral and boundary-element techniques [28].

To further distinguish dependence that is genuinely local from dependence enhanced by spatial mixing across the cavity, we introduce an additional random variable given by a coarse position label obtained by partitioning the cavity into spatial bins. This enables a position-conditioned characterization and the use of co-information (interaction information) as a compact measure of how spatial heterogeneity mediates the observed global amplitude–phase coupling [29].

The paper is organized as follows. We first introduce the open elliptical microcavity and the spectral signatures of the A.C. in the strong-interaction regime. We then define the Born-weighted amplitude–phase probability model and the associated information measures. Next we present the amplitude and phase entropy signatures across the A.C., and finally we introduce the coarse position label and co-information to disentangle within-

region dependence from spatial heterogeneity effects.

NON-HERMITIAN MODE INTERACTION AND AVOIDED CROSSING IN AN OPEN ELLIPSE

Non-Hermitian effective description and strong-interaction regime

Open wave systems are naturally described by non-Hermitian operators: radiative leakage and irreversible decay render the resonance spectrum complex, and the associated eigenmodes biorthogonal [1, 2]. In the vicinity of an exceptional point (EP), where both eigenvalues and eigenmodes coalesce, non-Hermitian effects become particularly pronounced and control the qualitative transition between weak and strong mode interaction [5, 6]. An open dielectric microcavity provides a convenient photonic platform to access this physics, because the leakage is intrinsic and can be tuned continuously by shape deformation [13].

Eliminating the bath degrees of freedom leads to an effective non-Hermitian Hamiltonian of the form

$$H = H_S + V_{SB} G_B^{(\text{out})} V_{BS}, \quad (1)$$

where H_S is the Hermitian operator of the corresponding closed system, $G_B^{(\text{out})}$ is the outgoing Green function in the bath, and V_{SB} (V_{BS}) describes the system-to-bath (bath-to-system) coupling. To connect this framework to the experimentally relevant spectral signatures, we use a minimal two-mode reduction parametrized by the eccentricity e ,

$$H(e) = \begin{pmatrix} \varepsilon_1(e) & v \\ v & \varepsilon_2(e) \end{pmatrix}, \quad \varepsilon_j(e) = \nu_j(e) - i\gamma_j(e), \quad (2)$$

with real coherent coupling $v \in \mathbb{R}$ and loss rates $\gamma_j \geq 0$. The eigenvalues are complex and can be written as

$$E_{\pm}(e) = \frac{\varepsilon_1(e) + \varepsilon_2(e)}{2} \pm Z(e), \quad (3)$$

where $Z(e) = \sqrt{[(\varepsilon_1(e) - \varepsilon_2(e))/2]^2 + v^2}$. In our microcavity setting, these complex eigenvalues correspond to the complex resonant wavenumbers $k = \Re(k) - i\Im(k)$ of the Helmholtz problem: $\Re(k)$ determines the resonance frequency while $\Im(k) > 0$ encodes the radiative loss rate.

Near resonance, the interaction regime is governed by the competition between coherent coupling and differential loss. One obtains a repulsion in $\Re(E_{\pm})$ with a crossing in $\Im(E_{\pm})$ for $2v > |\Im(\varepsilon_1) - \Im(\varepsilon_2)|$ (strong interaction), whereas $\Im(E_{\pm})$ repel with $\Re(E_{\pm})$ crossing for $2v < |\Im(\varepsilon_1) - \Im(\varepsilon_2)|$ (weak interaction). The boundary $Z(e) = 0$ corresponds to an EP and marks the transition between these two regimes. In our data, the observed spectral pattern is the strong-interaction case: a

clear avoided crossing in $\Re(k)$ accompanied by a crossing in $\Im(k)$ within the eccentricity window analyzed below. We note that the complementary weak-interaction case yields similar qualitative conclusions for the field-based information diagnostics developed in the following sections.

Open elliptical microcavity and spectral signatures

Having established the minimal non-Hermitian framework, we now specify the concrete wave system used throughout the paper and summarize the spectral signatures that identify the avoided crossing (A.C.) pair.

We study two-dimensional dielectric microcavities governed by the scalar Helmholtz equation for TM polarization,

$$(\nabla^2 + n^2 k^2) \psi(\mathbf{r}) = 0, \quad (4)$$

where $\psi(\mathbf{r})$ denotes the out-of-plane electric field (E_z) at position $\mathbf{r} = (x, y)$. The refractive index is piecewise constant, $n(\mathbf{r}) = n_{\text{in}} = 3.3$ inside the cavity and $n(\mathbf{r}) = n_{\text{out}} = 1$ outside. At the dielectric boundary we impose the standard TM interface conditions, i.e., continuity of ψ and of the normal derivative $\partial\psi/\partial n$, and in the exterior we enforce the outgoing (Sommerfeld) radiation condition. As a result, the resonant wavenumbers are complex, $k = \Re(k) - i\Im(k)$ with $\Im(k) > 0$ encoding radiative loss. We compute resonances and associated fields using a boundary element method (BEM), a boundary-integral scheme with outgoing Green's functions that naturally yields a non-Hermitian effective operator for open systems [28].

Throughout this work, the cavity boundary is taken to be an ellipse with semi-axes $a = (1 + \varepsilon)$ and $b = (1 + \varepsilon)^{-1}$, so that the area πab is fixed to π while the shape is controlled by the deformation parameter ε (with a the major and b the minor semi-axis). For later convenience we also introduce the corresponding eccentricity $e = \sqrt{1 - b^2/a^2}$ ($0 \leq e < 1$), which provides a one-to-one measure of the same shape deformation. In the present dataset we focus on the interval $e \simeq 0.669 - 0.687$, corresponding to the deformation window $\varepsilon \in [0.16, 0.173]$, which contains the avoided-crossing region analyzed in Fig. 1.

Figure 1(a) shows two interacting eigenmodes forming an A.C. pair: as e is varied, the two branches in $\Re(k)$ approach and repel, while the inset confirms a concomitant variation in $\Im(k)$. The six intensity snapshots A-F visualize the real-space manifestation of this coupling through $|\psi(\mathbf{r})|^2$. Far from the interaction window the two branches exhibit distinct intensity morphologies, whereas near the A.C. (B and E) the patterns become strongly hybridized. Crossing the A.C., the modal character is exchanged between the branches, consistent with the spectral repulsion in $\Re(k)$ and the correlated response of $\Im(k)$.

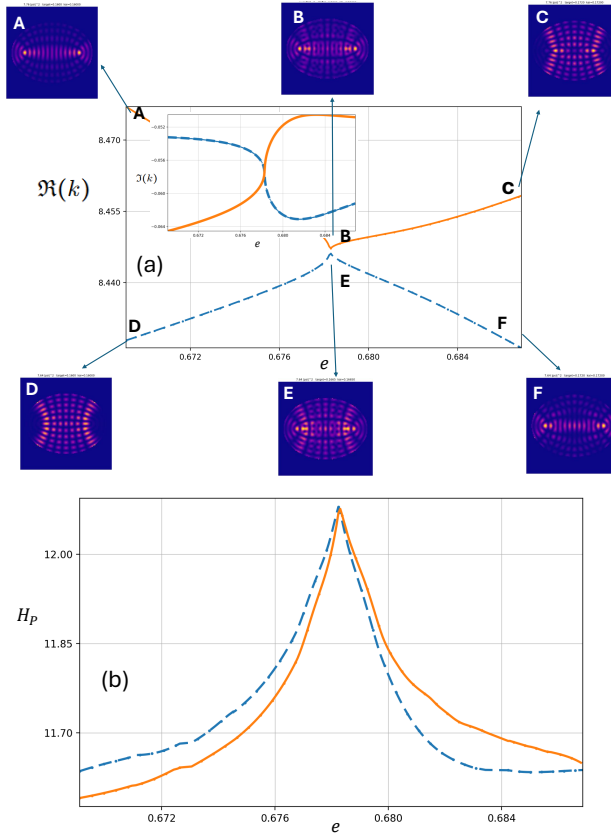


FIG. 1: Avoided crossing and intensity-based spatial entropy. (a) $\Re(k)$ of two interacting resonances versus eccentricity e (solid: mode 1; dashed: mode 2) shows a clear avoided crossing; the inset plots $\Im(k)$ in the same window. Intensity snapshots A–F illustrate strong hybridization near the A.C. (B,E) and exchange of modal character across it. (b) Shannon entropy H_P (bits) of the normalized spatial density $p(\mathbf{r}) = |\psi(\mathbf{r})|^2 / \sum_{\mathbf{r} \in \Omega} |\psi(\mathbf{r})|^2$ (cavity interior Ω) peaks near the A.C., quantifying enhanced delocalization of the *intensity* distribution.

To quantify the spatial redistribution associated with this spectral interaction, Fig. 1(b) plots the classical Shannon entropy H_P of the normalized spatial probability density $p(\mathbf{r}) = |\psi(\mathbf{r})|^2 / \sum_{\mathbf{r} \in \Omega} |\psi(\mathbf{r})|^2$, where $\mathbf{r} = (x, y)$ denotes the position on the cavity grid. By construction, $p(\mathbf{r}) \geq 0$ and it satisfies the normalization $\sum_{\mathbf{r} \in \Omega} p(\mathbf{r}) = 1$ over the cavity-interior grid points Ω . The entropy is evaluated in bits as

$$H_P = - \sum_{\mathbf{r} \in \Omega} p(\mathbf{r}) \log_2 p(\mathbf{r}), \quad (5)$$

where Ω denotes the cavity-interior grid points. Similar Shannon-entropy diagnostics of spatial mode redistribution have been used to characterize avoided crossings and exceptional points in open microcavities [30, 31], and have also been applied in other platforms such as confined atomic systems and acoustic superlattices [32–34].

In this context, H_P measures how broadly the inten-

sity $|\psi(\mathbf{r})|^2$ is spread over the cavity: larger H_P indicates stronger spatial delocalization of the mode intensity. Notably, H_P exhibits a pronounced peak in the A.C. region, aligning with the strong hybridization observed in panels B and E. Away from the A.C., H_P decreases as the intensity recovers a more structured and localized pattern, indicating that the entropy enhancement is tightly linked to mode mixing and the exchange of modal character across the avoided crossing.

The intensity-based entropy in Fig. 1(b) provides a coarse but robust marker of strong mode interaction in real space. While $|\psi(\mathbf{r})|^2$ is a gauge-invariant observable and thus experimentally robust, it discards the phase structure and the non-orthogonality (biorthogonality) that are intrinsic to non-Hermitian eigenmodes; these features become crucial precisely in the strong-interaction window near an EP. This motivates us to probe the complex field $\psi(\mathbf{r})$ itself through the joint statistics of its local amplitude $A(\mathbf{r}) = |\psi(\mathbf{r})|$ and phase $\Phi(\mathbf{r}) = \arg \psi(\mathbf{r})$, and to quantify their coupling via amplitude–phase information measures introduced next.

AMPLITUDE-PHASE PROBABILITY MODEL AND INFORMATION MEASURES

Born-weighted sampling and random variables on the cavity grid

While the spatial entropy H_P captures the redistribution of the *intensity* $|\psi(\mathbf{r})|^2$, openness renders the eigenmodes intrinsically non-Hermitian objects: they are generally biorthogonal and can exhibit reduced phase rigidity, especially near mode interaction and EP-related regimes [1, 2, 6]. This means that diagnostics based solely on $|\psi(\mathbf{r})|^2$ do not fully characterize the non-Hermitian eigenmode structure. Motivated by this, we analyze the complex *field* $\psi(\mathbf{r})$ at the level of its local amplitude $A(\mathbf{r}) = |\psi(\mathbf{r})|$ and phase $\Phi(\mathbf{r}) = \arg \psi(\mathbf{r})$, and quantify how their joint statistics evolve across the avoided crossing. Such amplitude–phase information measures provide a complementary handle on non-Hermitian mode mixing and offer a route toward diagnosing eigenmode properties beyond intensity-based observables. Related information-theoretic diagnostics of complex eigenmodes across avoided crossings in open microcavities have also been developed from complementary representations [35].

At this point it is important to clarify why we work with the amplitude–phase pair (A, Φ) rather than the Cartesian decomposition $\psi(\mathbf{r}) = \Re \psi(\mathbf{r}) + i \Im \psi(\mathbf{r})$. The latter is not invariant under a global $U(1)$ gauge rotation $\psi(\mathbf{r}) \mapsto e^{i\theta} \psi(\mathbf{r})$: a change of the arbitrary overall phase mixes $\Re \psi$ and $\Im \psi$ through a rigid rotation in the complex plane, and thus reshuffles any statistics built directly from the two components [35]. In contrast, the amplitude $A(\mathbf{r})$ is strictly gauge-invariant, and the phase $\Phi(\mathbf{r})$

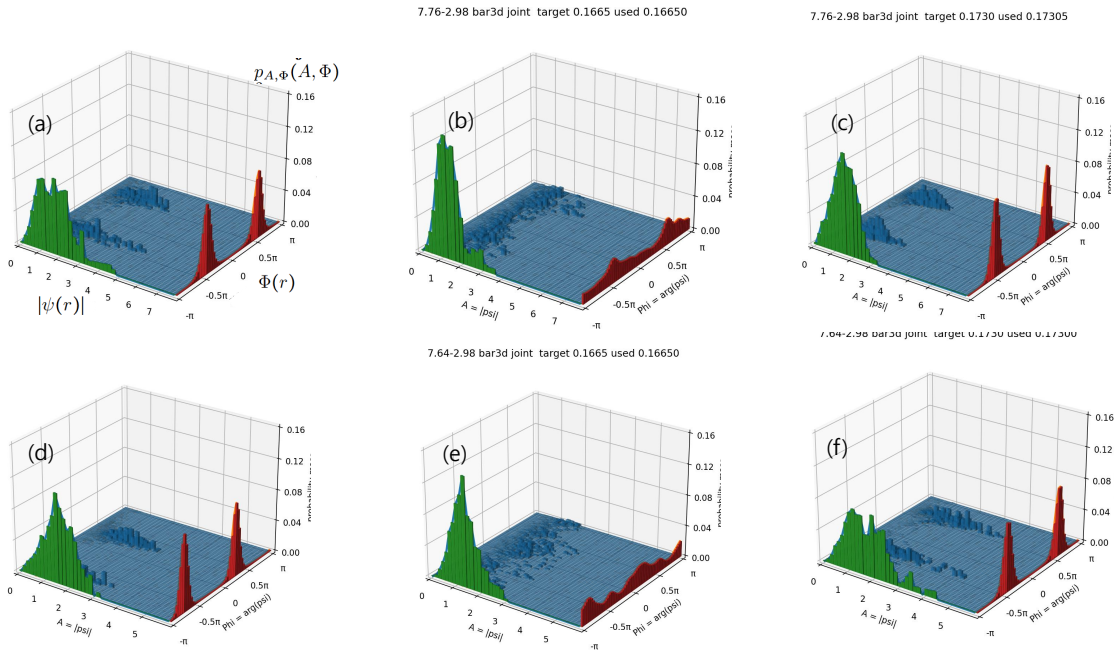


FIG. 2: **Born-weighted amplitude–phase joint distributions across the A.C.** Joint histograms show $p_{A,\Phi}(A,\Phi)$ from cavity-interior points weighted by $w(\mathbf{r}) = |\psi(\mathbf{r})|^2$, with $A(\mathbf{r}) = |\psi(\mathbf{r})|$ and $\Phi(\mathbf{r}) = \arg \psi(\mathbf{r}) \in [-\pi, \pi]$. Green/red walls are the marginals $p_A(A)$ and $p_\Phi(\Phi)$. Panels (a–c) follow points A–C on the upper branch and (d–f) points D–F on the lower branch in Fig. 1(a), with B and E at the A.C. At the A.C. (b,e), p_A narrows while p_Φ broadens, anticipating a local minimum of $H(A)$, an increase of $H(\Phi)$, and a peak of $I(A;\Phi)$.

transforms by a uniform shift $\Phi(\mathbf{r}) \mapsto \Phi(\mathbf{r}) + \theta$, so that physically meaningful phase diagnostics can be formulated either in terms of relative phases or circular statistics insensitive to the choice of global phase reference. This gauge-separation makes (A, Φ) a more robust representation for characterizing non-Hermitian eigenmodes, whose overall phase is generically unconstrained and can vary across parameter sweeps.

We now formalize the amplitude–phase statistics used in Figs. 2 and 3. Unlike the spatial entropy H_P , which depends only on the normalized density $p(\mathbf{r})$, the present analysis treats the local field observables as *random variables* induced by Born-weighted sampling on the cavity grid [25, 26]. For a given eigenmode, the *sample space* is the discrete set of cavity-interior grid points $\Omega = \{\mathbf{r}_1, \dots, \mathbf{r}_N\}$ with $\mathbf{r} = (x, y)$, and a single *outcome* is the selection of one grid point $\mathbf{r} \in \Omega$. Here Ω includes only cavity-interior grid points; exterior points by construction are excluded, while interior nodal points (zeros within the cavity) are retained. Throughout, grid points are sampled according to the normalized Born weight $P(\mathbf{r}) \propto |\psi(\mathbf{r})|^2$ on Ω .

The amplitude and phase are then random variables

on (Ω, P) , namely maps from the sample space of grid points to their respective *value spaces* (codomains),

$$A : \Omega \rightarrow \mathbb{R}_{\geq 0}, \quad A(\mathbf{r}) = |\psi(\mathbf{r})|, \quad (6)$$

$\Phi : \Omega \rightarrow [-\pi, \pi], \quad \Phi(\mathbf{r}) = \arg \psi(\mathbf{r}), \quad (7)$
 where $\mathbb{R}_{\geq 0}$ and $[-\pi, \pi)$ define the value spaces over which the amplitude and phase distributions are supported. The joint and marginal distributions of (A, Φ) are then the push-forward of P under the map $\mathbf{r} \mapsto (A(\mathbf{r}), \Phi(\mathbf{r}))$, i.e., the distribution of the values $(A(\mathbf{r}), \Phi(\mathbf{r}))$ induced by sampling $\mathbf{r} \sim P$.

Discretized joint distribution and Shannon-type measures (bits)

For numerical evaluation, we discretize $A \in [0, A_{\max}]$ into N_A bins $\{B_i\}$ and Φ into N_Φ circular bins $\{C_j\}$ on $[-\pi, \pi)$ (identifying $-\pi$ and π to avoid edge artifacts). The binned joint probability mass is computed by a Born-weighted 2D histogram,

$$p_{A,\Phi}(i,j) = \mathbb{P}(A \in B_i, \Phi \in C_j) = \frac{\sum_{r \in \Omega: A(r) \in B_i, \Phi(r) \in C_j} |\psi(r)|^2}{\sum_{r \in \Omega} |\psi(r)|^2}, \quad (8)$$

which satisfies $p_{A,\Phi}(i,j) \geq 0$ and $\sum_{i,j} p_{A,\Phi}(i,j) = 1$. The amplitude and phase marginals follow by summation,

$$p_A(i) = \sum_j p_{A,\Phi}(i,j), \quad p_\Phi(j) = \sum_i p_{A,\Phi}(i,j). \quad (9)$$

In our implementation we used $N_A = 300$ and $N_\Phi = 256$ bins. The upper amplitude cutoff A_{\max} was chosen globally for each dataset as

$$A_{\max} = \max_{\text{files}} \max_{r \in \Omega} |\psi(r)|, \quad (10)$$

so that all parameter-dependent curves are compared on the same amplitude discretization. We verified that the qualitative trends reported below are stable under reasonable variations of (N_A, N_Φ) .

From these discretized probabilities we compute Shannon-type information measures in bits (\log_2). The marginal entropies are

$$H(A) = - \sum_i p_A(i) \log_2 p_A(i), \quad (11)$$

$$H(\Phi) = - \sum_j p_\Phi(j) \log_2 p_\Phi(j), \quad (12)$$

and the joint entropy is

$$H(A, \Phi) = - \sum_{i,j} p_{A,\Phi}(i,j) \log_2 p_{A,\Phi}(i,j). \quad (13)$$

We emphasize the conditional entropies,

$$H(A|\Phi) = H(A, \Phi) - H(\Phi), \quad (14)$$

$$H(\Phi|A) = H(A, \Phi) - H(A), \quad (15)$$

and introduce the mutual information,

$$I(A; \Phi) = H(A) - H(A|\Phi) = H(\Phi) - H(\Phi|A), \quad (16)$$

which quantifies the statistical dependence between local amplitude and phase. With these definitions, we next track $H(A)$, $H(\Phi)$, $H(A, \Phi)$ and $I(A; \Phi)$ across the avoided crossing and relate their behavior to non-Hermitian mode mixing.

AMPLITUDE-PHASE SIGNATURES OF THE AVOIDED CROSSING

Distribution-level reshaping of $p_{A,\Phi}$ across the avoided crossing

Figure 2 provides a distribution-level view of the avoided-crossing (A.C.) response by visualizing the Born-weighted joint distribution $p_{A,\Phi}(A, \Phi)$ together with the marginals $p_A(A)$ and $p_\Phi(\Phi)$ at representative parameter points. Panels (a–c) correspond to the marked points

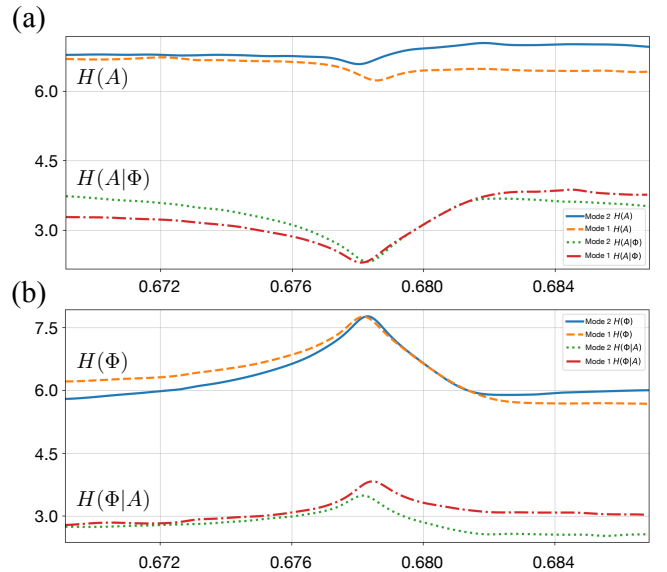


FIG. 3: **Amplitude and phase entropies across the avoided crossing.** (a) Amplitude entropy $H(A)$ and conditional amplitude entropy $H(A|\Phi)$ versus eccentricity e for the two interacting modes. Both curves exhibit a clear dip in the avoided-crossing (A.C.) window. (b) Phase entropy $H(\Phi)$ and conditional phase entropy $H(\Phi|A)$ versus e . Both curves form a pronounced peak in the same A.C. window. In both sectors, conditioning substantially reduces the entropy, demonstrating strong statistical dependence between local amplitude and phase under Born-weighted sampling.

A–C on the upper branch (mode 1) in Fig. 1(a), while panels (d–f) correspond to the marked points D–F on the lower branch (mode 2); in particular, B and E represent the A.C. points for the two branches.

A systematic reshaping occurs at the A.C. panels (b,e): the amplitude marginal $p_A(A)$ sharpens while the phase marginal $p_\Phi(\Phi)$ broadens. This redistribution at the level of the full joint distribution highlights that the strong-interaction window reorganizes the complex eigenfield in a way that cannot be inferred from intensity-only diagnostics. The entropy-based analysis below quantifies these distribution-level changes and separates their impact into the amplitude and phase sectors.

Entropic and correlational response: amplitude localization versus phase delocalization

The distribution-level changes in Fig. 2 translate into sharp information-theoretic signatures when quantified by the marginal and conditional entropies defined in Eqs. (11)–(15). In Fig. 3 we summarize the A.C. response for the two interacting modes, focusing here on the marginal and conditional measures of the amplitude and phase sectors.

Figure 3 quantifies the A.C. response using the mea-

sures introduced in Eqs. (11)–(15). The amplitude sector [Fig. 3(a)] exhibits a distinct dip in both $H(A)$ and $H(A|\Phi)$ in the A.C. window, indicating that the amplitude variable $A(r) = |\psi(r)|$ becomes more localized in its *value space* at the mixing point. This contrasts with the behavior of the intensity-based spatial entropy H_P (Fig. 1), which increases near the A.C. due to real-space hybridization and redistribution of $|\psi(\mathbf{r})|^2$. The two observations are logically consistent because real-space redistribution and value-space spreading are distinct notations: the A.C. can enhance spatial delocalization of the intensity pattern while simultaneously tightening the distribution of local amplitude values.

The most nontrivial signature appears in the phase sector. In non-Hermitian resonators, $|\psi(r)|^2$ discards the phase information entirely, so intensity-only observables cannot diagnose how the complex eigenfield reorganizes its phase. Figure 3(b) shows that the phase entropy $H(\Phi)$ reaches a pronounced maximum in the same A.C. window, demonstrating that $\Phi(r) = \arg \psi(r)$ becomes maximally delocalized in value space at the mixing point. Importantly, this phase broadening persists under conditioning: $H(\Phi|A)$ also peaks in the A.C. window, indicating that the phase delocalization is not a trivial byproduct of amplitude variations but reflects a genuine restructuring of the complex field in the strong-interaction regime.

A robust quantitative feature is that conditioning reduces the uncertainty by about a factor of two in both sectors: $H(A|\Phi) \approx \frac{1}{2}H(A)$ and $H(\Phi|A) \approx \frac{1}{2}H(\Phi)$, with the strongest contrast near the A.C. window. This shows that amplitude and phase are strongly dependent random variables under the Born-weighted sampling on Ω , so that specifying one variable significantly constrains the other. We will return to the two-variable characterization in the next section, where joint measures are discussed together with the integrated interpretation of the A.C. response.

POSITION-CONDITIONED AMPLITUDE-PHASE DEPENDENCE AND CO-INFORMATION

A coarse position label as a new random variable

Building on the Born-weighted sampling model on the cavity grid defined in the previous section, we introduce an additional random variable that encodes *where* in the cavity the field is sampled. We partition the (x, y) domain into 40×40 spatial bins $\{B_m\}_{m=1}^M$ with $M = 40^2$, and define the coarse position label

$$\Pi : \Omega \rightarrow \{1, \dots, M\}, \quad \Pi(\mathbf{r}) = \{m, \quad \mathbf{r} \in B_m\}. \quad (17)$$

Here \mathbf{r} is sampled from the same Born-induced probability mass function $P(\mathbf{r})$ as before, so the induced distri-

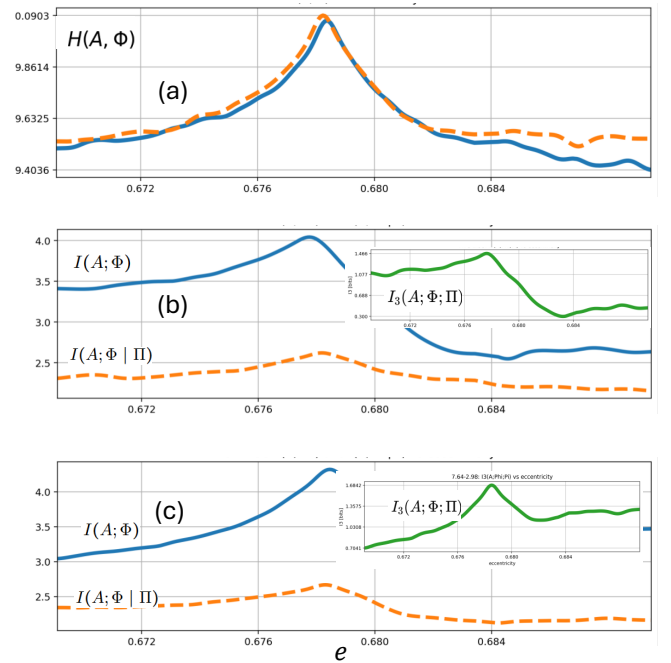


FIG. 4: **Joint entropy and position-conditioned amplitude-phase dependence across the avoided crossing.** (a) Joint entropy $H(A, \Phi)$ versus eccentricity e . (b,c) Global mutual information $I(A; \Phi)$ (solid) and position-conditioned mutual information $I(A; \Phi | \Pi)$ (dashed) versus e for the two datasets. Insets plot the co-information $I_3(A; \Phi; \Pi) = I(A; \Phi) - I(A; \Phi | \Pi)$. All information measures use base-2 logarithms and are reported in bits.

bution of Π is [25]

$$p_\Pi(m) = \mathbb{P}(\Pi = m) = \sum_{\mathbf{r} \in \Omega : \Pi(\mathbf{r}) = m} P(\mathbf{r}). \quad (18)$$

Thus, $p_\Pi(m)$ equals the Born-weighted probability mass carried by bin m , i.e., the fraction of the mode intensity contained in that coarse region. Bins with $p_\Pi(m) = 0$ carry no Born weight and do not contribute to any Π -conditioned quantities; equivalently, conditioning is understood on the support $\{m : p_\Pi(m) > 0\}$. In this sense, Π provides a physically transparent control variable that separates *within-region* amplitude-phase structure from *across-region* spatial heterogeneity.

Position-conditioned mutual information and co-information

We next ask how much of the global amplitude-phase dependence is retained when the coarse spatial label is specified. The position-conditioned mutual information is defined by [25]

$$I(A; \Phi | \Pi) = H(A | \Pi) + H(\Phi | \Pi) - H(A, \Phi | \Pi). \quad (19)$$

Equivalently, in terms of the Π -resolved distributions, it can be written as

$$I(A; \Phi | \Pi) = \sum_{m: p_{\Pi}(m) > 0} p_{\Pi}(m) \sum_{i,j} p_{A,\Phi|\Pi}(i, j | m) \log_2 \frac{p_{A,\Phi|\Pi}(i, j | m)}{p_{A|\Pi}(i | m) p_{\Phi|\Pi}(j | m)}. \quad (20)$$

To compare the global dependence to the within-bin dependence, we introduce the co-information (interaction information)

$$I_3(A; \Phi; \Pi) = I(A; \Phi) - I(A; \Phi | \Pi), \quad (21)$$

which is symmetric under permutation of the three variables [29, 36, 37]. If $I_3(A; \Phi; \Pi) > 0$, then conditioning on Π *reduces* the amplitude–phase dependence, indicating that a non-negligible portion of the global $I(A; \Phi)$ is attributable to mixing across spatial bins (spatial heterogeneity at the coarse scale). If $I_3(A; \Phi; \Pi) < 0$, the within-bin dependence is, on average, *stronger* than the globally mixed dependence, meaning that coarse spatial mixing partially masks locally strong amplitude–phase correlations.

CONCLUSION

We introduced a field-level, information-theoretic diagnostic of non-Hermitian mode interaction in an open elliptical microcavity across an avoided crossing. While the intensity-based spatial entropy peaks in the A.C. window, the complex field shows a complementary split: the amplitude entropy dips and the phase entropy peaks, with conditioning indicating strong amplitude–phase dependence. A coarse position label further shows that the enhanced global coupling near the A.C. is strongly shaped by spatial heterogeneity across the cavity. These diagnostics provide a compact route to identifying and comparing strong-interaction regimes in open resonators and can aid mode engineering and control in wave-based platforms where complex fields are computed or reconstructed (e.g., interferometric phase retrieval and Wigner/tomographic measurements).

ACKNOWLEDGEMENT

This work was supported by the National Research Foundation of Korea (NRF) through a grant funded by the Ministry of Science and ICT (Grants Nos. RS-2023-00211817 and RS-2025-00515537), the Institute for Information & Communications Technology Promotion (IITP) grant funded by the Korean government (MSIP)

(Grants No. RS-2025-02304540), and the National Research Council of Science & Technology (NST) (Grant No. GTL25011-401). S.L. acknowledges support from the National Research Foundation of Korea (NRF) grants funded by the MSIT (Grant No. RS-2022-NR068791).

* Electronic address: parkkw7777@gmail.com

† Electronic address: level@khu.ac.kr

‡ Electronic address: kgjeong6@snu.ac.kr

- [1] I. Rotter, “A non-Hermitian Hamilton operator and the physics of open quantum systems,” *J. Phys. A: Math. Theor.* **42**, 153001 (2009).
- [2] N. Moiseyev, *Non-Hermitian Quantum Mechanics* (Cambridge University Press, Cambridge, 2011).
- [3] Y. Ashida, Z. Gong, and M. Ueda, “Non-Hermitian physics,” *Adv. Phys.* **69**, 249–435 (2021).
- [4] H. Feshbach, “Unified theory of nuclear reactions,” *Ann. Phys. (N.Y.)* **5**, 357–390 (1958).
- [5] T. Kato, *Perturbation Theory for Linear Operators* (Springer, Berlin, 1966).
- [6] W. D. Heiss, “The physics of exceptional points,” *J. Phys. A: Math. Theor.* **45**, 444016 (2012).
- [7] M. V. Berry, “Physics of non-Hermitian degeneracies,” *Czech. J. Phys.* **54**, 1039–1047 (2004).
- [8] E. J. Bergholtz, J. C. Budich, and F. K. Kunst, “Exceptional topology of non-Hermitian systems,” *Rev. Mod. Phys.* **93**, 015005 (2021).
- [9] K. Ding, C. Fang, and G. Ma, “Non-Hermitian topology and exceptional-point geometries,” *Nat. Rev. Phys.* **4**, 745–760 (2022).
- [10] N. Okuma and M. Sato, “Non-Hermitian topological phenomena: A review,” *Annu. Rev. Condens. Matter Phys.* **14**, 83–107 (2023).
- [11] K. Vahala, ed., *Optical Microcavities* (World Scientific, Singapore, 2004).
- [12] T. Harayama and S. Shinohara, “Two-dimensional microcavity lasers,” *Laser Photon. Rev.* **5**, 247–271 (2011).
- [13] H. Cao and J. Wiersig, “Dielectric microcavities: Model systems for wave chaos and non-Hermitian physics,” *Rev. Mod. Phys.* **87**, 61–111 (2015).
- [14] M. Parto, Y. G. N. Liu, B. Bahari, M. Khajavikhan, and D. N. Christodoulides, “Non-Hermitian and topological photonics: optics at an exceptional point,” *Nanophotonics* **10**(1), 403–423 (2021).
- [15] H. Nasari, G. G. Pyrialakos, D. N. Christodoulides, and M. Khajavikhan, “Non-Hermitian topological photonics,” *Opt. Mater. Express* **13**(4), 870–885 (2023).

[16] C. Wang, Z. Fu, W. Mao, J. Qie, A. D. Stone, and L. Yang, “Non-Hermitian optics and photonics: from classical to quantum,” *Adv. Opt. Photon.* **15**(2), 442–523 (2023).

[17] B. Zhen *et al.*, “Spawning rings of exceptional points out of Dirac cones,” *Nature* **525**, 354–358 (2015).

[18] J. Doppler *et al.*, “Dynamically encircling an exceptional point for asymmetric mode switching,” *Nature* **537**, 76–79 (2016).

[19] W. Chen, S. K. Özdemir, G. Zhao, J. Wiersig, and L. Yang, “Exceptional points enhance sensing in an optical microcavity,” *Nature* **548**, 192–196 (2017).

[20] J. Wiersig, “Review of exceptional point-based sensors,” *Photonics Res.* **8**(9), 1457–1467 (2020).

[21] A. Li *et al.*, “Exceptional points and non-Hermitian photonics at the nanoscale,” *Nat. Nanotechnol.* **18**, 706–720 (2023).

[22] H. Meng, Y. S. Ang, and C. H. Lee, “Exceptional points in non-Hermitian systems: Applications and recent developments,” *Appl. Phys. Lett.* **124**(6), 060502 (2024).

[23] C. E. Shannon, “A mathematical theory of communication,” *Bell Syst. Tech. J.* **27**, 379–423, 623–656 (1948).

[24] E. T. Jaynes, “Information theory and statistical mechanics,” *Phys. Rev.* **106**, 620–630 (1957).

[25] T. M. Cover and J. A. Thomas, *Elements of Information Theory*, 2nd ed. (John Wiley & Sons, Hoboken, 2006).

[26] D. J. C. MacKay, *Information Theory, Inference, and Learning Algorithms* (Cambridge University Press, Cambridge, 2003).

[27] A. Kraskov, H. Stögbauer, and P. Grassberger, “Estimating mutual information,” *Phys. Rev. E* **69**, 066138 (2004).

[28] J. Wiersig, “Boundary element method for resonances in dielectric microcavities,” *J. Opt. A: Pure Appl. Opt.* **5**, 53–60 (2003).

[29] W. J. McGill, “Multivariate information transmission,” *Psychometrika* **19**, 97–116 (1954).

[30] K.-W. Park, S. Moon, Y. Shin, J. Kim, K. Jeong, and K. An, “Shannon entropy and avoided crossings in closed and open quantum billiards,” *Phys. Rev. E* **97**, 062205 (2018).

[31] K.-W. Park, J. Kim, S. Moon, and K. An, “Maximal Shannon entropy in the vicinity of an exceptional point in an open microcavity,” *Sci. Rep.* **10**, 12551 (2020).

[32] S. Saha and J. Jose, “Shannon entropy as a predictor of avoided crossing in confined atoms,” *Int. J. Quantum Chem.* **120**(22), e26374 (2020).

[33] J. Sánchez-Dehesa and J. R. Arias-Gonzalez, “Characterization of avoided crossings in acoustic superlattices: The Shannon entropy in acoustics,” *Front. Phys.* **10**, 971171 (2022).

[34] W. S. Nascimento, M. M. de Almeida, and F. V. Prudente, “Coulomb correlation and information entropies in confined helium-like atoms,” *Eur. Phys. J. D* **75**, 171 (2021).

[35] K.-W. Park, S. Lee, and K. Jeong, “Information-theoretic analysis of complex eigenmodes across avoided crossings in open microcavities,” *Phys. Lett. A* **571**, 131298 (2026).

[36] S. Watanabe, “Information theoretical analysis of multivariate correlation,” *IBM J. Res. Dev.* **4**(1), 66–82 (1960).

[37] A. J. Bell, “The co-information lattice,” in *Proc. 4th Int. Symp. Independent Component Analysis and Blind Sig-* *nal Separation (ICA2003)* (Nara, Japan, 2003), pp. 921–926.